

STUDIES OF AIRFLOW THROUGH A HUMAN NASOPHARYNX AND PHARYNX AIRWAY

H.F. LI¹, Z.F. TIAN¹, J.Y. TU¹, W. YANG², G.H. YEOH³, C.L. XUE⁴ and C.G. LI⁴

¹School of Aerospace, Mechanical and Manufacturing Engineering, RMIT University, Australia

²Division of Minerals, Commonwealth Scientific and Industrial Research Organization, Australia,

³Australian Nuclear Science and Technology Organization (ANSTO), PMB 1, Menai, NSW 2234, Australia

⁴School of Health Sciences, RMIT University, Australia

ABSTRACT

It has been proposed that certain pathological factors such as infection and smoking cause damage to extrathoracic tissue structures, thus contributing to clinical conditions in related diseases. Consequently, knowledge of airflow characteristics in the extrathoracic airway is essential to understand the physiology and pathology aspects of breathing. In this study, a computational fluid dynamics (CFD) technique is employed to model the low and high inspiration flows in part of the extrathoracic airway that comprises the nasopharynx bend and pharynx. Also, airflows are investigated experimentally by Particle Image Velocimetry (PIV). Calculated wall shear stresses by the numerical model indicated the prevalence of high values within the constricted planes of the pharynx region that can cause erosion of the surface layers leading towards possible malignancy tendencies. The quantitative airflow data will contribute to diagnosis and treatment, including surgical operation on extrathoracic airway diseases.

INTRODUCTION

The extrathoracic (EX) airway comprises five compartments: (i) nasal valve, (ii) nasal cavity, (iii) nasopharynx bend, (iv) pharynx and (v) larynx (Sarangapani and Wexler, 2000) (see Fig. 1). One of the main physiological functions of the EX airway is to cleanse the inspired air of pollutant particles, thereby protecting the delicate lower respiratory tract (Keyhani et al., 1995). Nevertheless, the exposed layer of soft tissues surrounding the airway are constantly subjected to possible lesions in cases through heavy smoking, which may increase the risk of contracting cancer. Cancer of the pharynx is the sixth most prevalent cancer worldwide, ranking third in the developing countries, and eighth in the developed world (Syrjänen, 2005). Other possible respiratory diseases such as asthma are also of major concern to the EX airway, which typically obstruct the airway due to hyper-responsiveness and possible inflammation of the lung airway epithelium (Djukanović et al., 1990).

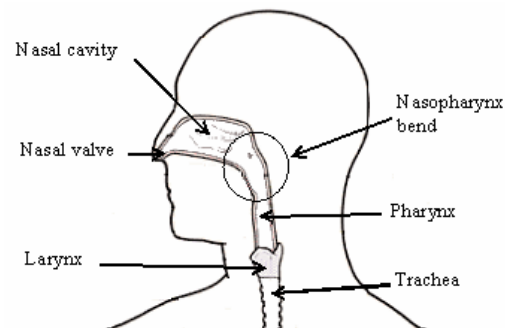


Figure 1. A schematic representation of the extrathoracic system.

With increasing computational resources and the widespread availability of Computational Fluid Dynamics (CFD) codes, the methodology is gaining in popularity as an attractive research tool to study the airflow pattern in the human respiratory system. Research such as Elad et al. (1993), Yu et al. (1998) and many others have exploited the use of CFD codes towards the prediction of airflow in the EX airway. Besides the academic interest, CFD also has the considerable potential and provision for clinical applications. Based on the realistic geometrical structure of the EX airway, CFD codes could provide detailed information of the wall shear stress, pressure drop, airflow rate, temperature distribution, and water vapor conditions.

Because of the application of approximate CFD models, the selection of the appropriate choice of turbulence models for biomedical applications requires investigation. The standard $k-\epsilon$ model, which is based on a two-equation approach (k is the turbulent kinetic energy and ϵ is the dissipation of the turbulent kinetic energy) commonly used in many engineering applications, has been demonstrated to perform rather poorly in predicting the EX flows (Stapleton et al., 2000). Zhang and Kleinstreuer (2003) evaluated other

turbulence models that included four Eddy-Viscosity turbulence Models (EVMs) and reported that the Low Reynolds Number (LRN) $k-\omega$ model (Wilcox, 1998) gave the best performance in predicting of the flow within the EX surrounding space. Here, ω is defined as the inverse of the dissipation ε . However, these EVMs have been found to be insensitive to the orientation of the turbulence structure, its transporting and mixing mechanisms (Hanjalic, 1994), and their inability to account for the selective amplification or attenuation of different Reynolds stresses by curvature-related strain components. Furthermore, the EVMs under-predicted the pressure-driven secondary flows and produced a weak, highly diffused streamwise vorticity field in simulating the flow in a 90° bend (Sotiropoulos and Ventikos, 1998). Thus, the suitability of EVMs for the EX airflow is doubtful due to the curvature streamline in the 90° nasopharynx bend where secondary flow and strongly anisotropy occur.

To overcome the above deficiencies associated with the EVMs, a second-order Reynolds Stress Model (RSM) is employed in the present analysis that solves the transport equations for each individual Reynolds stress. The RSM accounts automatically for the effects of streamline curvature and stress anisotropy. It usually performs better than EVMs in applications where the anisotropy of the Reynolds stresses dominates the flow (Hanjalic, 1994). Thus, the RSM may be more suitable for the EX airflow than the EVMs.

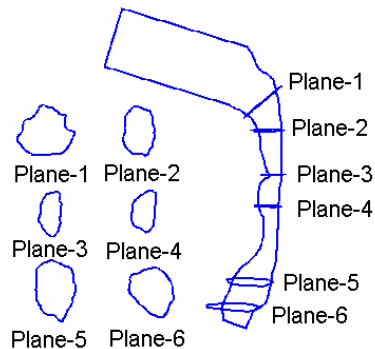


Figure 2. Simplified Extrathoracic airway geometry.

In this paper, an anatomically accurate geometry of a healthy male adult EX airway, which only comprises the nasopharynx bend and pharynx, has been successfully generated from CT scan images, as shown in Fig. 2. The anatomically accurate geometry of the airway is investigated both experimentally and numerically with the aim of better understanding the air flow characteristics around the 90° nasopharynx and other areas downstream. To validate of the numerical predictions, a physical flow passage is measured using the Particle Image Velocimetry (PIV)

technique. Descriptions and possible conclusions of the particular flow characteristics observed in these areas of the EX airway are discussed.

CREATION OF FLOW PASSAGE AND EXPERIMENTAL SETUP

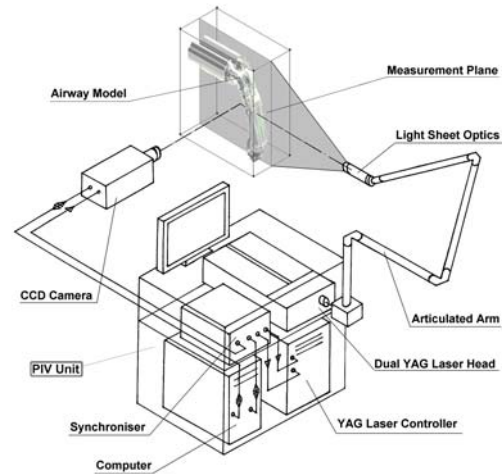


Figure 3. Schematic diagrams of the PIV apparatus.

In order to build a realistic physical model for experimental study, a computer model is created from CT scan image files. The image files are converted into three-dimensional volume files and then save as a stereolithography (STL) file, which is a standard format for further processing. Manufacturing based on the STL file is done using a Computer Numerical Control (CNC) machine and a solid copy of the flow passage in a transparent acrylic block is produced.

Figure 3 is a schematic diagram of the PIV apparatus. The single-phase fluid flow field within the airway was measured using 2D Particle Image Velocimetry (PIV). The ILA 2D PIV system consists of a 1.3Megapixel (1280×1024 pixels) 12-bit digital CCD camera which was synchronised with a New Wave 120 mJ double-cavity Nd:YAG laser. The laser beam was expanded by a cylindrical lens to form a 2mm thick plane vertical light sheet that was directed horizontally through the centre of the EX airway. The seeding particles used were TSI silver-coated hollow glass beads with mean diameter of $14\mu\text{m}$ and relative density of 1.65 to water.

NUMERICAL METHOD

A generic commercial CFD code, FLUENT, is utilized to predict the velocity profiles of the continuum gas phase under steady-state conditions through solutions to the conservation of mass and momentum. The

transport equation for the Reynolds stresses $-\overline{u'_i u'_j}$ is given by:

$$\begin{aligned} \frac{\partial}{\partial x_k} \left(\overline{u_k u'_i u'_j} \right) &= \left(\overline{u'_i u'_k} \frac{\partial u_j}{\partial x_k} + \overline{u'_j u'_k} \frac{\partial u_i}{\partial x_k} \right) - \frac{\partial}{\partial x_k} \left[\overline{u'_i u'_j u'_k} + \frac{p}{\rho} (\delta_{jk} u'_i + \delta_{ik} u'_j) \right] \\ \text{(i)} \quad \quad \quad \text{(ii)} \quad \quad \quad \text{(iii)} \\ + \frac{\partial}{\partial x_k} \left[\nu \frac{\partial}{\partial x_k} \left(\overline{u'_i u'_j} \right) \right] &+ \frac{p}{\rho} \left(\frac{\partial \overline{u'_i}}{\partial x_j} + \frac{\partial \overline{u'_j}}{\partial x_i} \right) - 2\nu \frac{\partial u_i}{\partial x_k} \frac{\partial u_j}{\partial x_k} \\ \text{(iv)} \quad \quad \quad \text{(v)} \quad \quad \quad \text{(vi)} \end{aligned} \quad (1)$$

The terms indicated in Eq. (1) that require no modeling are: (i) convection term, (ii) production and (iv) the molecular diffusion term.

For term (iii), a simplified scalar turbulent diffusivity is used to model the turbulent diffusive term (Lien and Leschziner, 1994):

$$-\frac{\partial}{\partial x_k} \left[\overline{u'_i u'_j u'_k} + \frac{p}{\rho} (\delta_{jk} u'_i + \delta_{ik} u'_j) \right] = \frac{\partial}{\partial x_k} \left(\frac{\nu_t}{\sigma_k} \frac{\partial \overline{u'_i u'_j}}{\partial x_k} \right) \quad (2)$$

where σ_k is with value of 0.82. ν_t is the turbulent kinematic viscosity defined as $\nu_t = C_\mu \frac{k^2}{\varepsilon}$. The turbulence kinetic energy k is obtained by $k = \frac{1}{2} \overline{u'_i u'_i}$ through the flow domain except for the boundary conditions.

The pressure-strain term (v) in Eq. (1) can be decomposed into three parts: a slow return to isotropy term $\Phi_{ij,1}$, a rapid return to isotropy term $\Phi_{ij,2}$ and the pressure-strain wall-echo term $\Phi_{ij,\omega}$. The slow return to isotropy term is modeled as

$$\Phi_{ij,1} = -C_1 \rho \frac{\varepsilon}{k} \left(\overline{u'_i u'_j} - \frac{2}{3} \delta_{ij} k \right) \quad (3)$$

where $C_1 = 1.8$. The rapid pressure-strain term is modeled as

$$\Phi_{ij,2} = -C_2 \left[(P_{ij} - C_{ij}) - \frac{2}{3} \delta_{ij} (P - C) \right] \quad (4)$$

where $C_2 = 0.6$ and P_{ij} and C_{ij} are respectively the stress production and convection terms: $P = \frac{1}{2} P_{kk}$ and

$C = \frac{1}{2} C_{kk}$. The pressure-strain wall-echo term $\Phi_{ij,\omega}$

redistributes the normal stresses near the wall by damping the normal stresses perpendicular to the wall while enhancing the stresses parallel to the wall. It is modeled as:

$$\begin{aligned} \Phi_{ij,\omega} &= C_1 \frac{\varepsilon}{k} \left(\overline{u'_k u'_m n_k n_m} \delta_{ij} - \frac{3}{2} \overline{u'_k n_j n_k} - \frac{3}{2} \overline{u'_j n_k n_k} \right) \frac{k^{2/3}}{C_1 \alpha d} \\ &+ C_2 \left(\overline{\phi_{km,2} n_k n_m} \delta_{ij} - \frac{3}{2} \overline{\phi_{jk,2} n_j n_k} - \frac{3}{2} \overline{\phi_{jk,2} n_i n_k} \right) \frac{k^{2/3}}{C_1 \alpha d} \end{aligned} \quad (5)$$

where the constants of C_1' and C_2' have values of 0.5 and 0.3 respectively. The variables n_k is the x_k component of the unit normal to the wall, d is the normal distance to the wall and $C_1 = C_\mu^{3/4} / K$ where K is the von Karman constant with a value taken as 0.4178.

The dissipation tensor (vi) in Eq. (1) is modeled by

$$-2\nu \frac{\partial u_i}{\partial x_k} \frac{\partial u_j}{\partial x_k} = \frac{2}{3} \delta_{ij} \varepsilon \quad (6)$$

The scalar dissipation rate ε is calculated according through a transport equation:

$$\frac{\partial}{\partial x_i} (\alpha u_i) = \frac{\partial}{\partial x_j} \left[\left(\nu + \frac{\nu_t}{\sigma_\varepsilon} \right) \frac{\partial \varepsilon}{\partial x_j} \right] + C_{\varepsilon 1} \frac{P_{ij} \varepsilon}{2k\rho} - C_{\varepsilon 2} \frac{\varepsilon^2}{k} \quad (7)$$

where $\sigma_\varepsilon = 1.0$, $C_{\varepsilon 1} = 1.44$ and $C_{\varepsilon 2} = 1.92$.

A computational mesh was generated enveloping the anatomical geometry, which was used to simulate the airflow. The computational domain contained initially 96,471 cells with 31,318 nodes. It was further refined and optimized after initial simulations, according to the geometrical complexity and flow conditions. The final domain contained 293,344 cells with 60,411 nodes. Further grid refinement indicated that a mesh of approximately 290,000 cells provided sufficient accuracy and resolution, which can be adopted as the base for future working grids.

The governing transport equations are discretised using the finite volume approach. The third order accurate QUICK scheme was used to approximate the convective terms, while the second-order-accurate central difference scheme is adopted for the diffusion terms. The pressure-velocity coupling was realized through the SIMPLE method.

RESULTS AND DISCUSSION

Comparison between PIV and CFD results

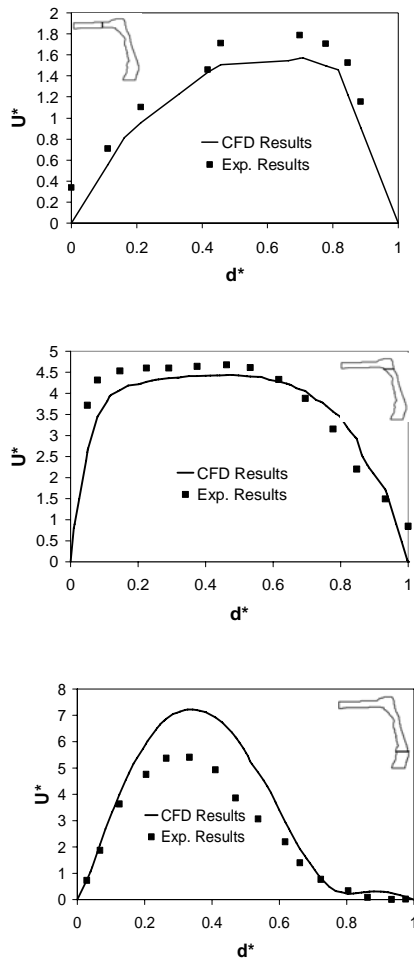


Figure 4. Comparison between PIV measurements and CFD predictions of streamline velocity profile at three locations.

The present CFD results have been compared with our experimental data. Fig. 4 shows streamline velocity profile at three different locations at the center-plane of the airway. d^* is dimensionless arc length, and u^* is velocity normalized by inlet velocity ($u^*=u/u_{in}$). There are some differences between the two results but overall the distribution and magnitudes of the mean velocities are very similar. With the quantitative comparison of PIV and CFD results, the good agreements instill confidence that the present CFD model is sufficiently accurate to analyze airflow in the EX airway.

Velocity and Turbulent Kinetic Energy

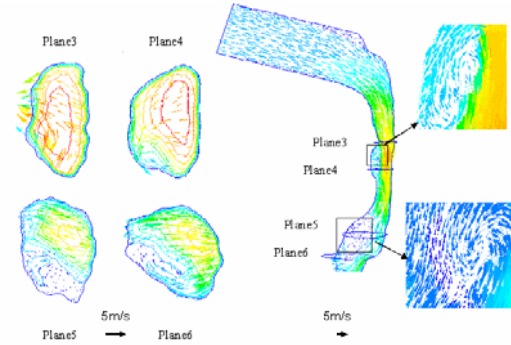


Figure 5 Velocity vectors at the different location along the EX airway.

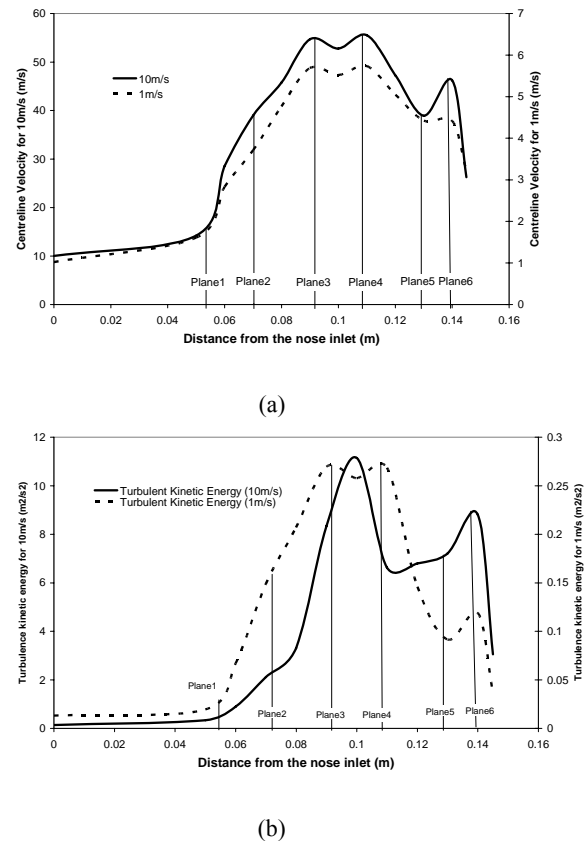


Figure 6. (a) Centerline velocity profile for inlet velocity; (b) Centerline turbulence kinetic energy profile for inlet velocity at 1m/s and 10m/s.

The mean centerline-velocity fields in the 90° nasopharynx bend, pharynx model under normal tidal aspiratory condition at low inhalation activity (1 m/s) are shown in Fig. 5. Different cross-sectional views of the airflows around the pharynx region indicated by planes 3 – 6 in Fig. 5 represent the axial velocity

contours as well as the secondary flow velocity vectors. The main characteristics of the depicted axial flow fields can be described by the following two distinct observations: (a) the velocity profiles became skewed in the curved portion of the pharynx due to centrifugal effects and (b) flow separation occurred with abrupt geometrical changes – the variation of cross-sectional area in the pharynx region. Because of the centrifugally induced pressure gradient, the secondary motion of the fluid persisted when the airflow turned the bend from the nose to the pharynx. The intensity of the secondary flows was strong, as demonstrated in the curved pharynx region (Planes 3, 4, 5 and 6). Fig. 6(a) illustrates the centerline velocity profiles in the airway for the cases of low inhalation (1 m/s) and high inhalation (10 m/s) activities that are within the range of normal breathing condition. Despite the differences in the velocity magnitudes, the trends of the velocity profiles recorded for the two activities were rather similar with the highest velocities achieved at Planes 3 and 4 of the pharynx region. These results demonstrated the independence of the velocity profiles on the inlet velocities; scaling of the velocities may be permissible for different range of inlet velocities. The maximum velocities recorded for either of the two inhalation activities were almost 5 times higher than the inlet velocities, indicating an acceleration of the airflow as it passed through the constricted areas of the pharynx region.

The variation of cross-sectional area-averaged turbulence kinetic energy as a function of the axial distance from the nose inlet is shown in Fig. 6(b). Substantial turbulence kinetic energy is generated, with maximum values of $0.25 \text{ m}^2/\text{s}^2$ and $10 \text{ m}^2/\text{s}^2$ located activities at planes 3 and 4 of the pharynx region. Regardless of either low or high inhalation activity, the turbulence kinetic energy increased dramatically after leaving Plane 1, around the 90° nasopharynx bend. It decreased from the maximum values as the flow of air traveled past the pharynx and increased again (Planes 5 and 6). The turbulence kinetic energy profiles were observed to be similar to those of the velocity profiles in Fig. 6(a).

Wall shear stress

The shear stress profiles calculated around the circumference wall of planes 3 and 4 are shown in Figs. 7. The circumferential direction is clockwise looking from the throat towards the flow inlet. As observed, there are substantial circumferential variations of the wall shear stress with the presence of peaks and valleys. At plane 3, the Wall Shear Stress (WSS) demonstrated a sharp peak at 10 Pa for an inlet velocity of 10 m/s while a maximum value of 0.5 Pa was achieved for an inlet velocity of 1 m/s. The predictions indicated that the maximum WSS occurred at the same location - a circumferential angle of 180° - regardless of the breathing situations. At the circumferential angle of 90° , the WSS also revealed high stress levels but marginally lower from those

experienced at the angle of 180° . Similar maximum magnitudes and behaviors were also observed at plane 4 in Fig. 7 at the circumferential angles of 90° and 180° albeit the absence of a marked dip of the WSS profiles between the angles of 90° and 180° , as portrayed in plane 3.

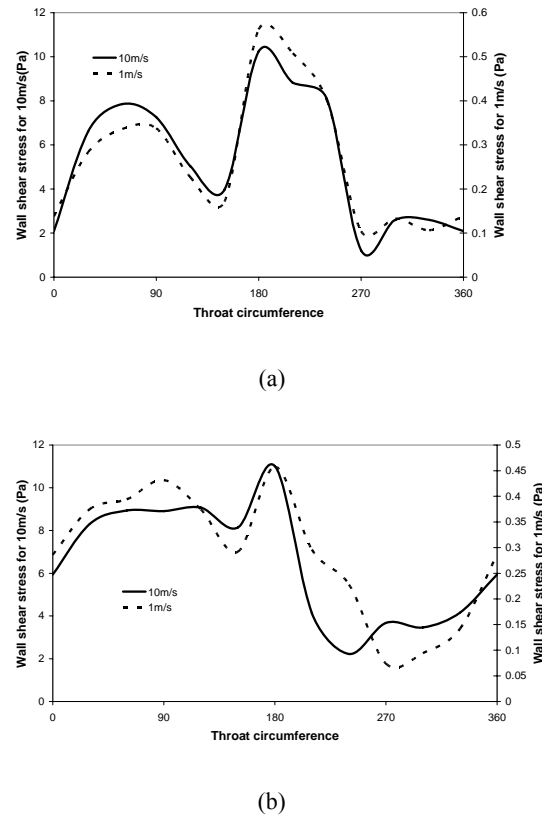
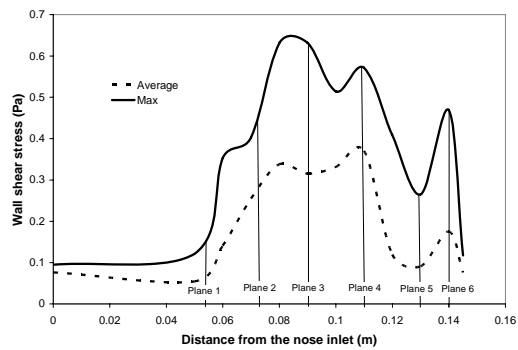


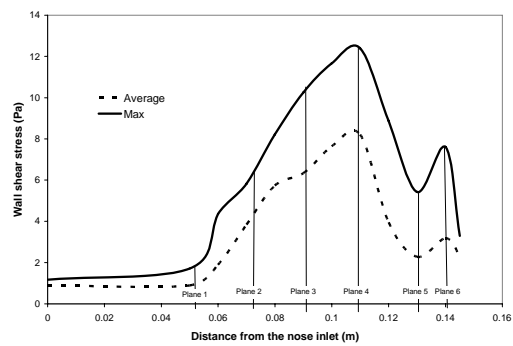
Figure 7 (a) Wall shear stress in Plane 3 for inlet velocity at 1m/s and 10m/s; (b) Wall shear stress in Plane 4 for inlet velocity at 1m/s and 10m/s.

The axially distributed average and maximum WSS profiles from the nose inlet to the trachea are presented in Fig. 8. The average values of the WSS have been obtained by spatially averaging the predicted circumferential surface stresses at incremental locations along the throat airway geometry. Here again, the WSS profiles were observed to be similar to the respective velocity and turbulence kinetic energy profiles in Fig. 6, though there is a high difference between the magnitudes. The dominantly high WSS concurred with the highest velocity and turbulent kinetic energy as the air passed through these constricted planes 3 and 4 of the pharynx region and planes 5 and 6 of the larynx region before flowing into the trachea. The distribution of these localized high WSS presents a strong case where they can cause surface lesions to the soft tissues surrounding the pharynx, thereby exposing unwanted

layers of sensitive and tender areas to possible infections. Thus, there is strong evidence that the erosion of these layers in the pharynx region has possible correlation with cancer, especially through heavy smoking. Malignant cells may develop through local inflammation of these regions. Frequent localizations of these surface lesions may continue to exacerbate the problem by the possibility of reaching a severe carcinomas state if they are left untreated.



(a)



(b)

Figure 8 Centerline wall shear stress profile for inlet velocity at (a) 1m/s and (b) 10m/s.

CONCLUSION

The RSM has shown to better capture the characteristics of strong secondary flow, anisotropy of shear stresses and curved streamline within the complex geometrical structure of part of the anatomical EX airway comprising of the 90° nasopharynx, pharynx. The topography of velocity, turbulent kinetic energy and WSS in the entire airway was determined under normal breathing conditions. The computational model revealed a substantial difference in both of the magnitude and spatial distribution of the velocity, turbulent kinetic energy and WSS values everywhere within the airway. This study particularly showed the existence of high WSS values that also concurred with high velocities and turbulent kinetic energy levels in the pharynx region. The presence of high WSS in the pharynx region is anatomic locations predisposed for possible lesion development. These lesions on the layers of soft

tissues surrounding the pharynx region expose the surfaces to possible infection and inflammation especially for cases of heavy smoking, which may increase the risk of contracting cancer because of the formation of malignant tumors.

ACKNOWLEDGEMENTS

The financial support provided by the Australian Research Council (project ID LP0347399) is gratefully acknowledged.

REFERENCES

- DJUKANOVIĆ, R., ROCHE, W.R., WILSON, J.W., BEASLEY, C.R.W., TWENTYMAN, O.P., HOWARTH, P.H., HOLGATE, S.T., 1990, Mucosal inflammation in asthma. *American Review of Respiratory Disease* 142, 434-457.
- ELAD D., LIEBENTHAL R., WENIG B.L., 1993. Analysis of air flow patterns in the human nose. *Medical, Biological Engineering and Computing* 31, 585-592.
- HANJALIC K., 1994. Advanced turbulence closure models: a review of current status and future prospects. *International Journal of Heat and Fluid Flow*. 15, 178-203.
- KEYHANI K., SCHERER P.W., MOZELL M.M., 1995. Numerical simulation of airflow in the human nasal cavity. *Journal of Biomechanical Engineering* 117, 429-441.
- LEIN F.S., LESCHZINER M.A., 1994. Assessment of Turbulent Transport Models Including Non-Linear RNG Eddy-Viscosity Formulation and Second-Moment Closure. *Computers and Fluids*, 23(8):983-1004, 1994
- SARANGAPANI R., WEXLER A.S., 2000. Modeling particle deposition in extrathoracic airways. *Aerosol Science and Technology* 32, 72-89.
- STAPLETON K.W., GUENTSH M.K., HOSKINSON M.K., FINLAY W.H., 2000. On the suitability of k-ε turbulence modeling for aerosol deposition in the mouth and throat: a comparison with experiment. *Journal of Aerosol Science* 6, 739-749.
- SOTIROPOULOS F, VENTIKOS Y., 1998. Flow through a curved duct using nonlinear two-equation turbulence models. *AIAA Journal* 36, 1256-1262.
- SYRJÄNEN, S., 2005. Human papillomavirus (HPV) in head and neck cancer. *Journal of Clinical Virology* 32S, S59-S66.
- WILCOX D.C., 1998. *Turbulence modeling for CFD*, 2nd ed. DCW Industries, Inc. La Canada, 103-217.
- YU G., ZHANG Z., LESSMAN R., 1998. Fluid flow and particle diffusion in the human upper respiratory system. *Aerosol Science and Technology* 28, 146-158.
- ZHANG Z, K and KLEINSTREUER C., 2003. Low-Reynolds-number turbulent flows in locally constricted conduits: a comparison study. *AIAA Journal* 41, 831-840.